



Experimental characterisation of rotor noise in tandem configuration

Alper Celik^{a,c,*}, Nur Syafiqah Jamaluddin^{b,c}, Kabilan Baskaran^{c,d}, Stefano Meloni^e,
Djamel Rezgui^c, Mahdi Azarpeyvand^c

^a Department of Aerospace Engineering, Swansea University, Swansea, SA1 8EN, UK

^b Jaguar Land Rover, Banbury Road, Gaydon, Warwick, CV35 0RR, UK

^c Department of Aerospace Engineering, University of Bristol, Bristol, BS8 1TR, UK

^d Department of Mechanical Engineering, Indian Institute of Technology (Indian School of Mines), Dhanbad 826004, India

^e Department of Economics, Engineering, Society and Business Organization, University of Tuscia, Viterbo, IT 01100, Italy

ARTICLE INFO

Keywords:

Rotor noise
Aeroacoustics
Tandem
Wind tunnel experiment
Urban air mobility

ABSTRACT

This paper presents a comprehensive investigation into the noise radiation characteristics of two rotors in a tandem configuration. Through an extensive experimental campaign, the study explores the effect of the separation distance between two rotors on the noise directivity patterns, spectral characteristics and temporal features of the radiated noise under both hovering and edge-wise flight conditions. The directivity patterns of the overall sound pressure level obtained from the polar and side arrays demonstrate a dependence on the separation distance and advance ratio. Spectral characteristics elucidate the influence of separation distance on tonal and broadband energy content. While the high-frequency broadband noise increases for both hovering and edge-wise flight similarly, the low-frequency broadband energy strongly depends on the advance ratio and the rotor separation distance. The results reveal a distinct envelope in the design space, where the radiated broadband noise for tandem configurations can be minimized, offering potential insights for noise reduction strategies. Additionally, the wavelet analysis for tandem configurations reveals that the emitted noise at the first and second blade passing frequency is strongly intermittent with amplitude modulation, which shall be considered for annoyance perception.

1. Introduction

The last decade has witnessed a tremendous effort from the scientific community to improve air transport across the globe through Urban Air Mobility (UAM). Manned and unmanned UAM technologies aim to revolutionise civil transportation, rescue operations, medical supply, and surveillance sectors. With the help of fast-growing electric propulsion technology, the multi-rotor distributed electric Vertical Take-off and Landing (eVTOL) vehicle market became one of the most competitive sectors. The challenge of developing electrified UAM vehicles does not necessarily arise from the aerodynamics perspective but also from the acoustics perspective. One main target for the UAM sector is improving urban mobility vehicles for public acceptance [1,2]. The goal to minimise the noise pollution from Vertiports, where the UAM vehicles take off and land, is challenged by the broad design space of the aircraft design with a unique noise signature for each vehicle [2–4].

The literature on large-scale VTOL, such as helicopters' aerodynamics and aeroacoustics, is well established [5–8]. However, helicopter noise theories may be applied directly to eVTOL vehicles (such as air taxis and drones) since UAMs may have more complicated layouts with multiple small-scale rotors designed to work at lower Reynolds numbers at lower velocities. The potential flow approximations used to design and optimise large-scale rotors with high Reynolds numbers are not proven to be valid for rotors employed for eVTOLs and drones. Studies in literature have addressed the issue of degraded hover performance of small-scale rotary wings compared to large-scale counterparts, such as helicopters [9,10]. Several investigations to understand the flow physics on small-scale rotors evidence stall cells, laminar separation bubbles (LSB) and turbulent transition on the wings [11–13]. Studies showed that tripping the rotor can eliminate the LSB and associated detrimental effects on aerodynamics [14]. Furthermore, a comprehensive experimental study showed the Re number dependency of aerodynamic performance, i.e., thrust and power coefficients, which was not observed

* Corresponding author.

E-mail addresses: alper.celik@swansea.ac.uk (A. Celik), syafiqah.jamaluddin@bristol.ac.uk (N. Syafiqah Jamaluddin), kabilan@iitism.ac.in (K. Baskaran), stefano.meloni@unitus.it (S. Meloni), djamel.rezgui@bristol.ac.uk (D. Rezgui), m.azarpeyvand@bristol.ac.uk (M. Azarpeyvand).

<https://doi.org/10.1016/j.apacoust.2024.110053>

Received 26 October 2023; Received in revised form 28 March 2024; Accepted 28 April 2024

Available online 16 May 2024

0003-682X/© 2024 The Author(s). Published by Elsevier Ltd. This is an open access article under the CC BY license (<http://creativecommons.org/licenses/by/4.0/>).

for a full-scale rotor [15], followed by a slipstream study to explore the effect on the vehicle as well as the other aircraft in wake [16–18].

Similar knowledge transfer difficulties are also evident in aeroacoustics, where the existing literature is built on helicopter investigations. The noise sources for a rotor are mainly classified into two main groups, i.e., tonal noise and broadband noise [7,19–23], and are identified with several driving mechanisms depending on the flight conditions and stage. The tonal noise (discrete-frequency noise) is generated due to steady loading, thickness discrete, blade vortex interaction and impulsive motion [24]. Broadband noise component has dipolar nature [25] and arises due to self-noise, i.e., turbulent boundary layer interaction with trailing edge, interaction with turbulence ingestion, and blade wake interaction noise [20]. For rotors in helicopters operating at high Reynolds number (Re) and tip Mach numbers, tonal noise is identified as the dominant component at low frequencies. In contrast, the broadband noise dominates at mid-to-high frequencies [8,24,26]. For small-scale propellers, Mach and Re numbers decrease significantly, and the flow regime over the blades significantly varies compared to large-scale blades. Recent studies, which primarily target understanding the noise characteristics of small-scale rotors for hover and forward flight conditions, conclude that, unlike helicopters, broadband noise at low-to-mid frequencies is significant [27–33]. It is worth noting that the tonal noise components, i.e., thickness and loading noise, have monopolar and dipolar behaviour, respectively [25].

The small-scale rotors employed in the emerging UAM market result in vehicle design with multiple rotors and propellers due to low lift and propulsion generation capacity. The layout of the rotors varies vastly for each design in conjunction with the purpose of the vehicle [34]. These multi-propeller-powered vehicles create complex flow interactions and noise radiations. Shukla and Narayanan [35] performed static tests, i.e., no freestream flow, for two side-by-side rotors and showed that close proximity of rotors at low Re numbers degrades the aerodynamic performance due to high inter-rotor wake interactions. The addition of the inflow at low speeds showed that vortices emanating from rotors interact more at higher Re numbers [36]. Zhou et al. [37] and Chae et al. [38] experimentally showed that the interaction between rotors enhances the force unsteadiness with no significant effect on the average values. Misiorowski et al. [39] investigated the rotor interactions for a quadcopter for two different layouts in edge-wise flight and explored the aerodynamic performance of each rotor. Vries et al. [40] investigated the aerodynamic interaction between propellers in various layouts for forward flight scenarios and demonstrated that an induced in-plane velocity component creates loading variations on the blade, which supports the observations in previous studies.

The impact of complexions in the flow field echoes in aeroacoustic investigations and understanding. Studies under static trust for a multirotor drone show that nonharmonic noises are as crucial as harmonic noises generated by the rotor [41]. Furthermore, the authors show the intermittent characteristics of the noise generated at the first blade passing frequency, attributing it to quadratic interactions and subtle differences in motor speeds. Poggi et al. [42] examined the Mach number scalability effect on the aeroacoustics numerically and showed that the emitted noise is scalable with the blade tip Mach number. Furthermore, the authors demonstrated that in the case of counter-rotating propellers, the phase between propellers could be manipulated to attenuate the noise radiation. Bu et al. [43] studied the effect of separation distance on noise radiation with a side-by-side propeller rig in a propulsion state. The study showed that the noise radiated by a dual propeller could be estimated by superimposing the noise radiated by each propeller, except for the observers at the wake region. Reed et al. [44] investigated the effect of both the vertical and horizontal separation distance between two rotors in static conditions, and in contrast to previous observations, showed that the OASPL levels are higher than two isolated rotors. Afari and Mankbadi [45] performed an extensive numerical study to address multi-rotor noise generation for hovering and forward flight scenarios. The study demonstrates a significant increase

in broadband noise and a modification of tonal noise compared to a single-rotor case for the hover case due to intense vortex generation and interaction between the gaps of the rotors. For forward flight conditions, the increased interaction between propellers due to convection enhances the noise radiation.

The present investigation provides a comprehensive experimental analysis of noise generated by small-scale rotors in the tandem configuration under hovering and edge-wise flight conditions compared to a single rotor case. The study aims to explore the effect of the stream-wise separation distance between rotors on the acoustic signature to provide design guidelines for UAM vehicles and experimental data for prediction tools. Furthermore, the study also investigates the intermittency characteristics of the generated noise via time-frequency analysis due to its importance for annoyance perception. The paper is organized as follows. Section 2 introduces the experimental set-up, tandem rotor rig, and instrumentation with brief details of post-processing techniques. Section 3 provides a detailed discussion of the results in three sub-sections. Section 3.1 presents the overall sound pressure directivity results, followed by Sec. 3.2 with details of the noise spectrum. Section 3.3 presents results on the time-dependent nature of the radiated noise. Lastly, the paper is concluded in Sec. 4 with some future remarks.

2. Experimental methodology

The experiments were performed at the University of Bristol's Aeroacoustic facility. The chamber is anechoic down to 160 Hz with physical dimensions of 6.7 m x 4.0 m x 3.3 m. The nozzle had a contraction ratio of 8.4:1 and had dimensions of 500 mm in width and 775 mm in length, which allows a steady operation from 5 m/s to 45 m/s and normal turbulence intensity levels below 0.2% [46].

Two identical rotor rigs were utilized to achieve the tandem configuration. The schematics of the rig are presented in Fig. 1. Each rig had an off-the-shelf 10"x5" two-bladed Graupner electric propeller. The rotors were driven by a 24-pole T-Motor Antigravity MN4006 brushless motor powered by a DC bench power supply. The rotational speed of the rotors was measured with an ICP Laser Tachometer. The separation distance, S , between rotors was varied $0.2R < S < 1.2R$ with an increment of $0.2R$. For brevity, the results and discussions are presented for the separation distances of $S = 0.2R, 0.6R$ and $1R$ compared to a single rotor case. The rotor rotational speed was fixed at 6000rpm. In order to address a broad range of operational envelope, the wind tunnel speed was varied between $0 \text{ m/s} < U < 24 \text{ m/s}$, which corresponds to an advance ratio range of $0 < \mu < 0.3$. Advance ratio is defined as,

$$\mu = \frac{U}{\Omega R}, \quad (1)$$

where Ω is the rotational speed, R is the radius of the blade and U is the free stream velocity.

Far-field noise measurements were obtained using 35 1/4 inch GRAS 40PL microphones, which have a large dynamic range and an upper limit of 142 dB, covering a frequency range between 10 Hz and 20,000 Hz. Two far-field arrays were used to obtain both the polar and side planes of sound radiation. These microphones were arranged onto a far-field array arc, allowing measurement between 40° and 150° polar angles at a distance of 1.75 m from the centre of the rotor system. A second side array spanning the angles between 110° and 240° at 1 m distance was also used. All the results were distance corrected to 1 m distance. All microphones were calibrated using a GRAS 42AA piston-phone calibrator. The far-field noise data were acquired using a National Instruments PXIe-1082 data acquisition system. Matlab R2016a was used to interface between the data acquisition system and the microphones to run the data acquisition code. The noise measurements were performed for 16 s at a sampling frequency of 2^{16} Hz.

The noise results are presented in terms of the frequency-dependent energy content of the pressure fluctuations. The energy content is expressed in terms of dB/Hz and is calculated as $10 \log_{10} \left(\phi_{pp} / p_{ref}^2 \right)$,

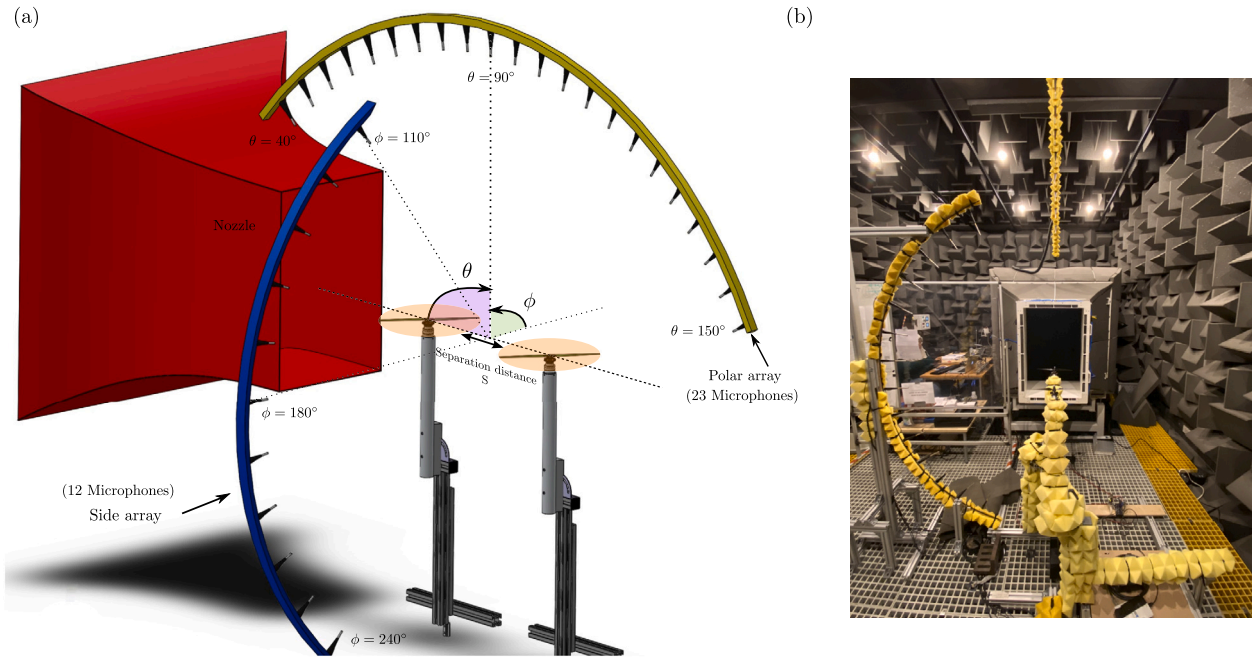


Fig. 1. (a) Schematics of the test rig with angle definitions, (b) Image of the experimental facility and rig.

where ϕ_{pp} is the power spectral density of the measured far-field pressure fluctuations, and $p_{ref} = 20 \mu\text{Pa}$ is the reference sound pressure. The power spectral density of the pressure fluctuations (ϕ_{pp}) was estimated by using Welch's method [47], where the data from the transducers are segmented for 32 equal lengths with 50% overlap and windowed by the Hamming function, resulting to a frequency resolution of $\Delta f = 2 \text{ Hz}$. The data obtained yields an absolute uncertainty of $\pm 0.05 \text{ dB}$ with a 95% of confidence level. Hereafter, $10 \log_{10} \left(\frac{\phi_{pp}}{p_{ref}^2} \right)$ will be referred to as power spectral density (PSD) for brevity. The overall sound pressure level (OASPL) was estimated by integrating the energy spectrum over the range of 90 Hz to 16 kHz as,

$$OASPL = 10 \log_{10} \left(\frac{\int PSD(f) df}{p_{ref}^2} \right). \quad (2)$$

The last part of the analysis was performed in the time-frequency domain employing wavelet transform to analyze intermittent events. The wavelet transform was applied by projecting the acquired signal onto the basis of compact support functions localized in the time domain and the transformed space. Formally, the wavelet transform of a time signal, in this case, the pressure signal $p(t)$, was defined as the inner product between $p(t)$ and the wavelet family $\psi(t)$ [48,49]:

$$w(s, \tau) = s^{-1/2} \int_{-\infty}^{\infty} p(t) \psi^* \left(\frac{t-\tau}{s} \right) dt, \quad (3)$$

where $s \in \mathfrak{R}^+$ was the scale dilation parameter, whose inverse corresponds to the frequency. $\tau \in \mathfrak{R}$ was the translation parameter corresponding to the position of the wavelet in the physical space, and $\psi^* \left(\frac{t-\tau}{s} \right)$ was the complex conjugate of the dilated and translated mother wavelet $\psi(t)$. For the sake of clarity all the results will be reported with respect to frequency.

In order to highlight the predominance and the intermittent behaviour of the detected signatures, the obtained wavelet coefficient was normalized with respect to the maximum value obtained in the time domain for each frequency as,

$$w^*(f, \tau) = \frac{|w(f, \tau)|^2}{\max(|w(BPF, \tau)|^2)}, \quad (4)$$

where $\| \cdot \|$ denotes absolute value.

3. Results and discussions

In this section, the far-field noise measurement results are presented and discussed in detail. In order to identify the overall effect of employing two rotors in tandem configuration with varying streamwise separation distances, a comparison of OASPL directivity is presented. The effect of separation distance on the noise characteristics is elaborated with extensive discussions of BPF directivity, spectrum analysis and time-frequency (wavelet) analysis. The experiments were conducted for separation distances of $0.2R < S < 1.2R$ and for incoming velocities of $0 \text{ m/s} < U < 24 \text{ m/s}$. However, the discussion primarily focuses on the results obtained at $S = 0.2R, 0.6R$ and $1R$ for brevity and their representative nature of the noise radiation patterns. Nonetheless, the results pertaining to other separation distances and incoming velocities are included in some of the figures to enhance the discussion when necessary.

3.1. Overall sound pressure level directivity

Far-field OASPL directivity results obtained from the polar and side microphone arrays are presented to provide an overall understanding of the radiated noise. Fig. 2 shows the far-field OASPL directivity results measured on the polar microphone array at four different advance ratios $\mu = 0, 0.1, 0.15$ and 0.2 at three separation distances in comparison with the results of a single (isolated) rotor. In the case of the hover condition, $\mu = 0$, the OASPL directivity pattern for all configurations, including the single rotor, displays a dipolar behaviour. The dipolar nature of the directivity demonstrates that loading noise and broadband noise dominate the far-field behaviour [25]. The OASPL results for all the tandem configurations exhibit a significant increase compared to the single rotor case, i.e., $\approx 6 \text{ dB/Hz}$, consistent with the previous observations [50].

The dipolar directivity pattern observed for the hover case ($\mu = 0$) is evident for all edge-wise flight cases, $\mu = 0.1, 0.15$ and 0.2 , and are presented in Fig. 2b, c and d. When the rotors are subjected to an incoming flow, i.e., $\mu = 0.1$ (Fig. 2b), the quick decay of noise radiation at the extremes of the polar angles becomes milder, and the difference between

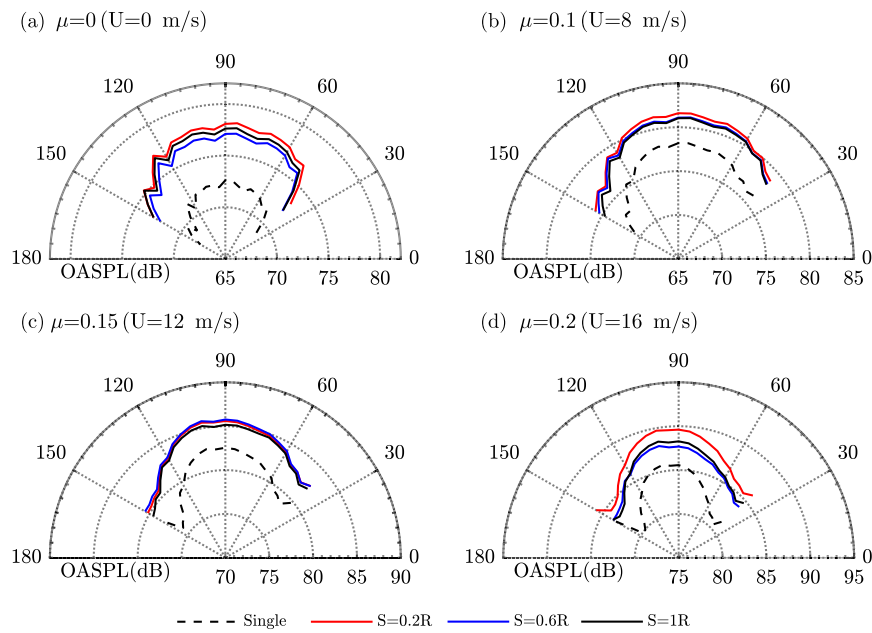


Fig. 2. OASPL directivity on polar array for separation distances of $S=0.2R$, $0.6R$ and $1R$ in comparison to single rotor results at an advance ratio of (a) $\mu=0$ (0 m/s), (b) $\mu=0.1$ ($U=8$ m/s), (c) $\mu=0.15$ ($U=12$ m/s) and (d) $\mu=0.2$ ($U=16$ m/s).

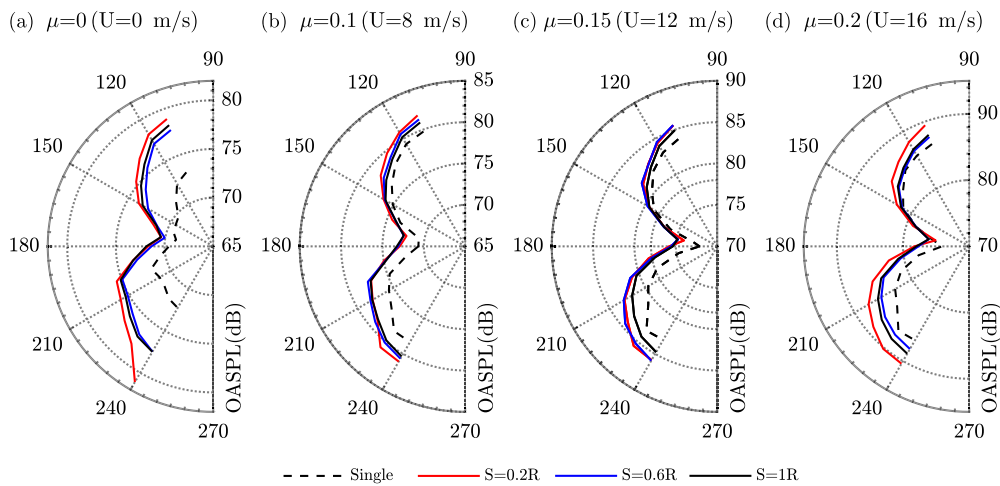


Fig. 3. OASPL directivity on side array for separation distances of $S=0.2R$, $0.6R$ and $1R$ in comparison to single (isolated) rotor results at advance ratios of (a) $\mu=0$ (0 m/s), (b) $\mu=0.1$ ($U=8$ m/s), (c) $\mu=0.15$ ($U=12$ m/s) and (d) $\mu=0.2$ ($U=16$ m/s).

the single rotor and tandem configurations reduce to less than 5 dB/Hz. Notable differences emerge at higher advance ratios where the peak of the dipolar pattern tilts downstream, accompanied by a marked increase of the far-field noise for the separation distance of $S=0.2R$. The tilt of the peak location on the directivity pattern may be attributed to the asymmetric flow domain exacerbated with the incoming flow. A similar directivity pattern is evident in the $\mu=0.15$ case. Although the single rotor radiates significantly less noise than the tandem configurations, there is no discernible difference among the tandem configurations regarding the directivity patterns or the OASPL. However, at $\mu=0.2$, the tilted directivity pattern becomes more pronounced. Furthermore, the $S=0.2R$ case radiates significantly higher noise, while the $S=0.6R$ case radiates slightly lower noise compared to the other tandem cases. Although not shown here for brevity and to align the study with practical applications regarding incoming flow speed, it is worth noting that as the inflow speed increases, the noise radiation for $S=0.6R$ cases becomes comparable to the single rotor case. These results are consistent with the findings in [44], where the authors assert that the fluid interaction between rotors shows a complex pattern and cannot be re-

duced to a function of the rotor separation distance, i.e., the smaller gap between rotors does not necessarily radiate higher levels of noise.

The results obtained from the side array support the dipolar nature of the noise radiation observed in all cases at all advance ratios. Unlike the results observed on the polar array, the OASPL difference between the single rotor and tandem configurations is less pronounced except in the $\mu=0$ case. The noise levels are slightly higher at the bottom quadrant of the array $180^\circ < \phi < 270^\circ$, which might be a footprint of increased wake interaction. The OASPL is significantly higher for the $S=0.2R$ case at $\mu=0.2$ compared to other tandem cases across most observation angles. Additionally, it is worth noting that results for $S=0.6R$ case are slightly lower compared to the results of the other configurations at $\mu=0.2$ for $180^\circ < \phi < 240^\circ$. These observations of increased far-field noise are consistent with the literature [44,45], where the increase in the noise is attributed to complex rotor wake interactions.

3.2. Spectral characteristics

In this section, the spectral characteristics of the noise emitted by both a single rotor and tandem configurations are addressed by pre-

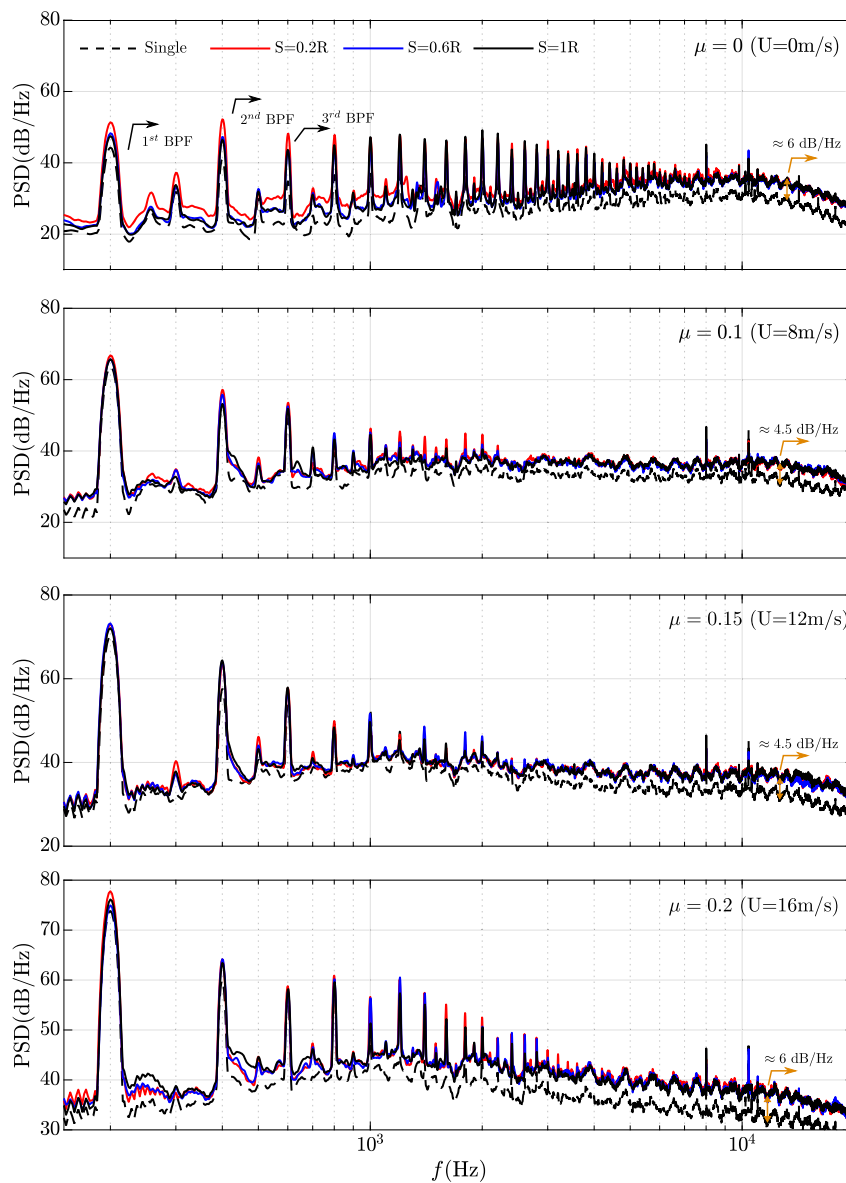


Fig. 4. Comparison of the far-field noise PSD of tandem configurations for separation distances of $S = 0.2R$, $0.6R$ and $1R$ against single rotor measured on the polar array at $\theta = 90^\circ$ for advance ratios of $\mu = 0$, 0.1 , 0.15 and 0.2 .

senting the individual power spectrum density of the sound pressure observed at the microphone $\theta = 90^\circ$ and $\phi = 120^\circ$. Furthermore, contour plots of the spectrum across the range of separation distances and advance ratios that were tested are provided for a comprehensive discussion. The directivity of the 1st BPF is also addressed due to its significance in terms of annoyance and perception [51]. Discussions on the noise spectra will involve two main components, i.e., the tonal contribution, which is due to blade passing frequency, and the broadband contribution, which is due to rotor self-noise, wake and turbulence interaction. It is worth noting that the contribution of thickness noise is negligible in the present study due to the small Mach number.

Fig. 4 displays the power spectral density (PSD) of the pressure fluctuations measured at $\theta = 90^\circ$ on the polar array at $\mu = 0$, 0.1 , 0.15 and 0.2 . The PSD is estimated as $10\log_{10}[(\phi_{pp}/p_0^2)]$, where ϕ_{pp} is the energy spectra calculated by Welch's method [47] and p_0 is the reference pressure ($20 \mu\text{Pa}$). Focusing on the tonal components of the spectra, i.e., behaviour around BPF and its harmonics, it is evident that the peaks of discrete tones dominate the low-to-mid frequencies. At the hover condition, i.e., $\mu = 0$, the dominant nature of tonal components diminishes around $f = 3000 \text{ Hz}$ for the single rotor case (dash line). Additionally,

a significant level of tonal noise persists at the higher harmonics of the BPF for all tandem cases for all advance ratios. It is worth noting that the high energy harmonics over a broad frequency range observed at $\mu = 0$ case is attributed to blade-vortex interaction in literature [11,52]. At the 1st BPF, the $S = 0.2R$ case radiates significantly higher noise compared to the other cases. Moreover, the elevated noise levels from the $S = 0.2R$ case persist at the higher harmonics until approximately $f \approx 1000 \text{ Hz}$. The rich nature of tonal noise is also evident at higher advance ratios. It is worth noting that with the introduction of flow, the radiated noise levels show a marked increase at the 1st BPF compared to the hover case (about 30 dB/Hz for $\mu = 0.2$ case). Across all advance ratios, the $S = 0.2R$ case radiates higher noise. Additionally, the behaviour at higher harmonics demonstrates a complex pattern and can not be easily generalized. However, it is worth noting that the tonal signature shows faster decay toward higher frequencies for most cases across all advance ratios compared to the results of the $\mu = 0$ case.

Having discussed the tonal behaviour, it is now pertinent to address the broadband component of the radiated noise. The broadband noise can be further categorized into low-frequency broadband noise (LFBN) and high-frequency broadband noise (HFBN) [53]. The HFPB noise may

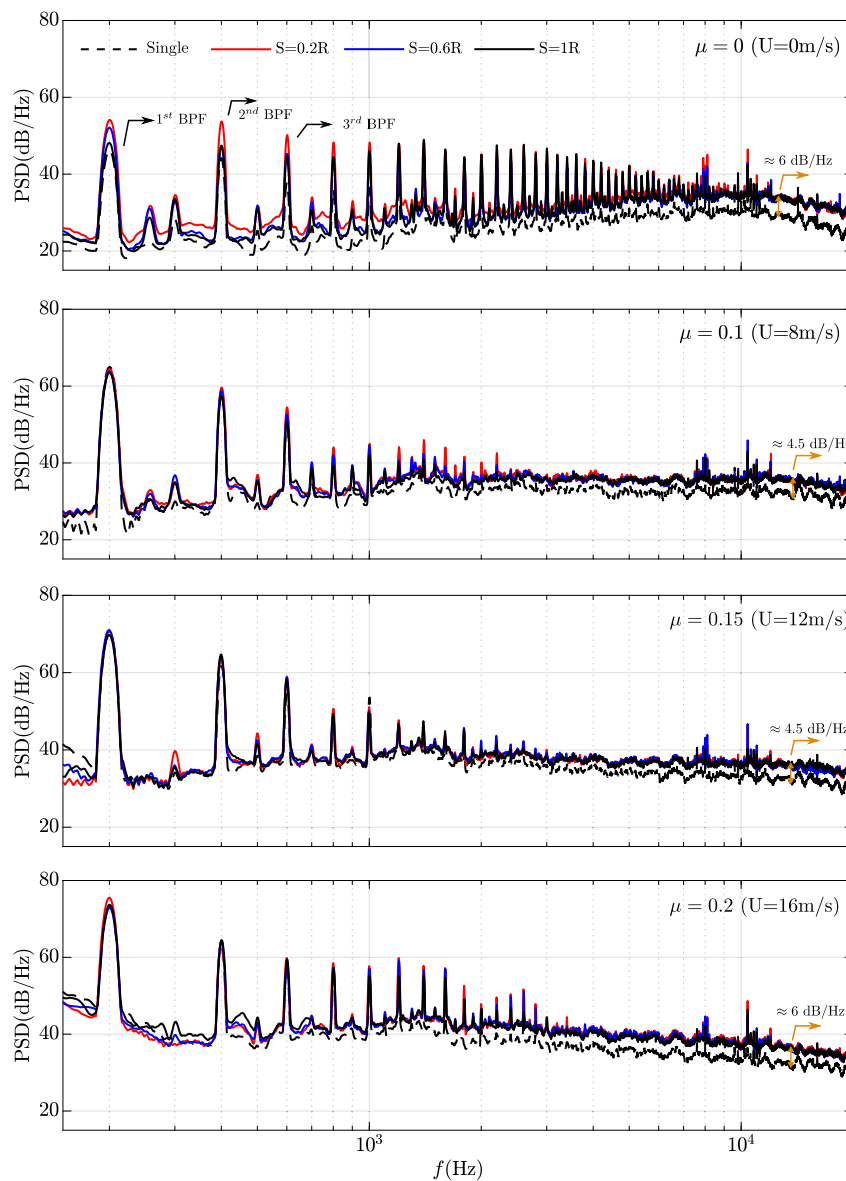


Fig. 5. Comparison of the far-field noise PSD of tandem configurations for separation distances of $S = 0.2R$, $0.6R$ and $1R$ against single rotor measured on the polar array at $\phi = 120^\circ$ for advance ratios of $\mu = 0$, 0.1 , 0.15 and 0.2 .

arise from various mechanisms such as boundary layer self-noise, turbulent boundary layer noise and incident turbulence noise. On the other hand, the LFBN is due to random loading, which may be attributed to wake interaction or inflow turbulence [54,55]. For the tandem case, the interaction of rotor wakes, both in the hover case and forward flight cases, is expected to contribute to the broadband component. Comparing the PSD results at mid-to-high frequencies, $f > \approx 4000$ Hz, a 6 dB/Hz increase of PSD is evident for all tandem cases across all advance ratios, compared to the single rotor case. A closer examination of lower frequencies at the hover case reveals some interesting phenomena. Above $f \approx 300$ Hz, an increase in the low-frequency broadband energy content is evident for all tandem cases. Moreover, the $S = 0.2R$ case exhibits a marked difference, $\approx 3 - 4$ dB/Hz, compared to other separation distances. The elevated broadband noise, particularly at low frequencies, may indicate increased wake interaction between rotors.

The presence of the incoming flow has a notable impact on the broadband behaviour of the PSD curves. For $\mu > 0$, the broadband energy distribution becomes similar for all tandem configurations. A discernible broadband hump emerges at mid-to-low frequencies, i.e., $500 \text{ Hz} < f < 3000 \text{ Hz}$. Moreover, higher inflow velocities develop

a more prominent hump with a shift towards lower frequencies, as demonstrated in Fig. 4(c) and (d). The observed broadband hump at low-to-mid frequencies may be attributed to wake interaction. However, a similar low-frequency broadband hump is also evident in the single rotor case with a considerably lower magnitude. Based on these observations, it can be inferred that a significant amount of the low-frequency broadband hump arises from the rotor's self-interaction with its wake, as indicated by the single rotor results, and a quantifiable magnitude arises due to rotor-rotor interaction. The low-frequency interaction noise peaks at $\mu = 0.2$ and decreases at $\mu = 0.3$ (not shown here for brevity). This variation in the noise levels may be due to the nature of the interaction and requires further flow field analysis. However, such a detailed flow field analysis goes beyond the scope of this manuscript. On the side array, Fig. 5, the PSD results are similar to those obtained from the polar array. During hovering, the $S = 0.2R$ case radiates the highest noise at the 1st BPF. Moreover, a discernible difference from the polar array results is that the $S = 0.6R$ case also radiates noise at a comparable level to the $S = 0.2R$ case. The elevated energy at low frequencies mirrors the polar array results. The presence of the flow introduces a low-frequency broadband hump, but

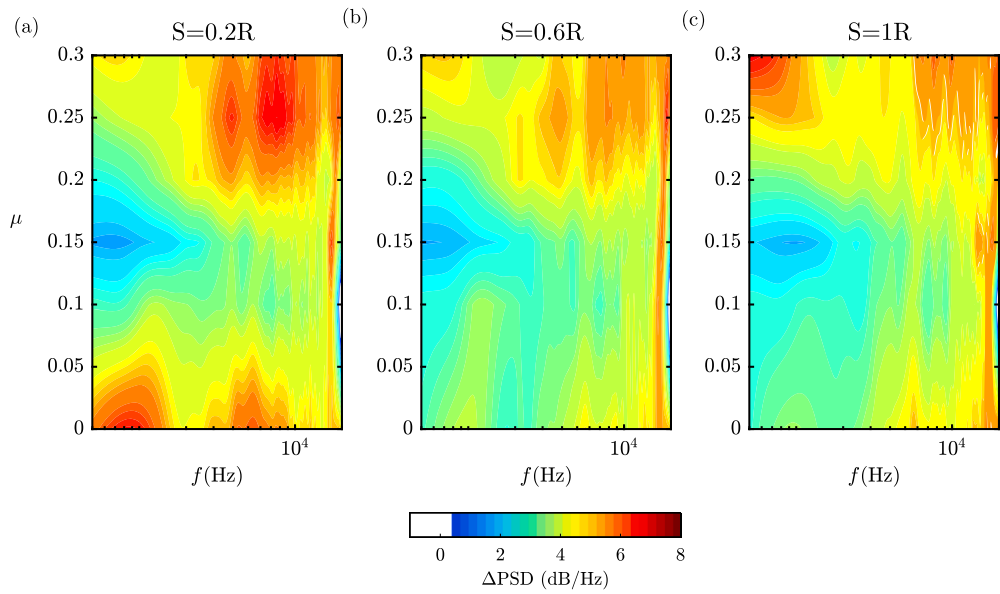


Fig. 6. Comparison of change in broadband noise with respect to the single rotor case [$\Delta\text{PSD} = (\text{PSD}_S - \text{PSD}_{\text{Single}})$] for (a) $S = 0.2R$, (b) $S = 0.6R$, and (c) $S = 1R$, over the advance ratio range of $0 < \mu < 0.3$.

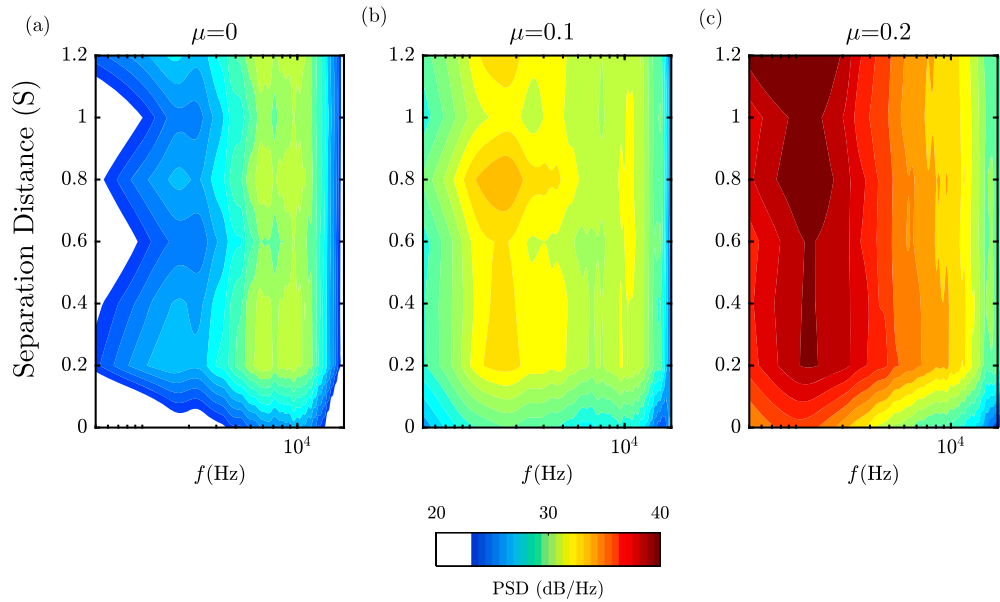


Fig. 7. Comparison of change in broadband noise at advance ratios (a) $\mu = 0$, (b) $\mu = 0.1$, and (c) $\mu = 0.2$ for the single rotor ($S = 0$), and over the separation distance range of $0.2R < S < 1.2R$.

lower in magnitude compared to the hover case. It is worth noting the results regarding the noise spectra obtained at $\phi = 230^\circ$ (presented in Supplementary document, Figure S1), which can be attributed to noise perceived at the ground. The general trend of the spectral content is similar to the spectra measured at $\phi = 120^\circ$ across all advance ratios. However, at $\mu = 0$, the maximum noise radiation at the 1st BPF is from the $S = 1R$ case as opposed to the $S = 0.2R$ case for $\phi = 120^\circ$. An overall comparison of the directivity and spectra results across Figs. 2 to 5 reveals that the $S = 0.2R$ case radiates significantly higher noise compared to $S = 0.6R$ and $S = 1R$ cases, with accompanied elevated levels of 1st BPF tonal noise across most advance ratios. Furthermore, the lowest excess noise (OASPL) compared to a single rotor is achieved by the $S = 0.6R$ case due to a lower broadband noise signature.

Figs. 6 and 7 are presented to investigate further the effect of the separation distance and advance ratio over the broadband far-field noise radiation measured on the polar array at $\theta = 90^\circ$. Fig. 6 displays the

PSD difference between tandem cases, i.e., $S = 0.2R, 0.6R$ and $S = 1R$ and the single rotor case over all the advance ratios tested, namely, $\mu = 0, 0.1, 0.15, 0.2, 0.25$ and $\mu = 0.3$. For this analysis, the broadband component of the spectrum is extracted through a median filter for each case [56–59]. Once the broadband component is obtained, ΔPSD is calculated as the difference between tandem cases and the single rotor case. A quick observation of the contour plots reveals positive values over the entire domain, indicating that tandem configurations generate higher broadband noise than the single rotor case, regardless of separation distances and advance ratios. Moreover, for all cases, the high-frequency content increases with higher inflow velocities, i.e., the advance ratio μ , as expected due to an increase in the trailing edge noise of the rotors.

At $S = 0.2R$, Fig. 6(a), the broadband noise increase is around 4–6 dB/Hz for most of the contour plot. ΔPSD map reveals a significant increase in broadband noise at low-to-mid frequencies for low advance

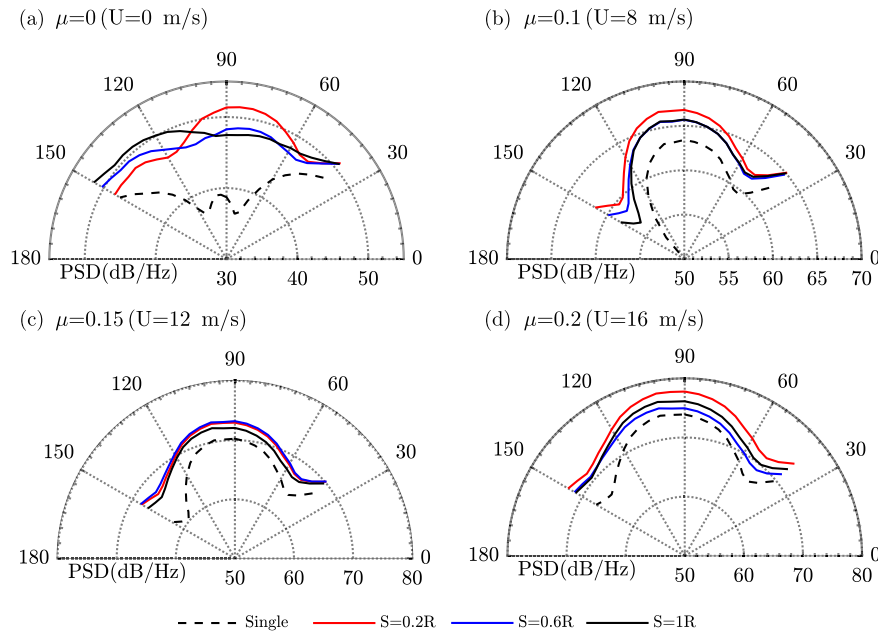


Fig. 8. 1st BPF directivity on the polar array for separation distances of $S = 0.2R$, $0.6R$ and $1R$ in comparison to single rotor results at advance ratios of (a) $\mu = 0$ (0 m/s), (b) $\mu = 0.1$ (8 m/s), (c) $\mu = 0.15$ (12 m/s) and (d) $\mu = 0.2$ (16 m/s).

ratios and at high frequencies for high advance ratios. Notably, at all separation distances, the increase in noise weakens at around $\mu = 0.15$ for low frequencies. Increasing the separation distance reduces the excess broadband noise over the entire spectra and advance ratios. Further increasing the separation distance to $S = 1R$ leads to a slight increase in ΔPSD at mid-to-high frequencies. Additionally, elevated broadband noise is evident at mid-frequencies for higher advance ratios. Considering the results in conjunction with the wake interaction, it appears that there exists a critical advance ratio envelope where the interaction reduces, and the radiated access noise compared to a single rotor case partially decreases. This suggests that certain separation distance and advance ratio combinations may mitigate the excess broadband noise resulting from wake interactions in the tandem configurations. For all separation distances, the excess noise is minimised over $0.05 < \mu < 0.2$ for the frequency range of $500 \text{ Hz} < f < 2000 \text{ Hz}$. For this operational envelope, the excess noise is 3 dB/Hz or lower. The excess noise ΔPSD is higher than 5 dB/Hz for all separation distances for $\mu > 0.2$. It is worth noting a few points regarding the low excess noise envelope observed at $\phi = 230^\circ$ for the broadband component following the previous discussions in Fig. 5. The ΔPSD results at $\phi = 230^\circ$ (presented in Supplementary document, Fig. S2) corroborate the observations in Fig. 6 where the lowest excess noise achieved around $0.1 < \mu < 0.2$. Furthermore, for $S = 0.6R$ and $S = 1R$ cases, the low excess noise region expands to higher and lower advance ratios over a broader range of frequencies.

To provide a comprehensive view of the separation distance effect on the far-field noise across different advance ratios, contour plots displaying the broadband PSD values over all separation distances tested at different advance ratios, i.e., $\mu = 0, 0.1$ and $\mu = 0.2$ are displayed. Fig. 7 illustrates the broadband PSD of the noise at advance ratios $\mu = 0, 0.1$ and $\mu = 0.2$ for all cases, starting from the single rotor case, $S = 0$ (Single), to all separation distances tested, $0.2R < S < 1.2R$. A remarkable finding from the results is the shift of mid-to-high frequency noise radiation to low-to-medium range noise radiation with the introduction of the inflow, which convects the slipstream towards the downstream rotor. Since the turbulence interaction noise is known to be a low-to-mid frequency range phenomenon [60], the shift of the dominant region of the spectrum can be attributed to the interaction of the downstream rotor with the wake of the upstream rotor. In addition, at a high ad-

vance ratio, the increase in the low-frequency broadband noise expands its bandwidth. This further highlights the impact of the separation distance and advance ratio on the broadband noise characteristics in the tandem configurations.

Before moving on to time-frequency analysis of the noise signatures, the directivity pattern at the maximum tonal noise, the 1st BPF, is also presented. Figs. 8 and 9 display the directivity patterns at the 1st BPF for polar and side array, respectively. It is worth noting that to allow a better interpretation of the results, the scales of the figures are not kept constant. At first glance, as the advance ratio increases, the radiated noise at the 1st BPF increases for all cases. Moreover, the directivity patterns do not show a radical change for edge-wise flight cases, Fig. 8(b-d). However, significant differences in the directivity patterns are evident among the hovering cases, as well as between the hovering and edge-wise flight cases. Considering the hovering case, $\mu = 0$, all tandem cases radiate more noise than the single rotor case. Among tandem cases, the highest far-field noise is radiated by $S = 0.2R$ case around $80^\circ < \theta < 100^\circ$. In contrast, the $S = 1R$ case radiates more noise downstream around $120^\circ < \theta < 150^\circ$. Inflow significantly changes the directivity pattern compared to the static case. An evident decay at the extremes of the dipolar pattern is observed for all cases. Moreover, the elevated PSD level for the $S = 0.2R$ case becomes more apparent compared to the results of the $S = 0.6R$ and $S = 1R$ cases. At $\mu = 0.2$, all cases display a similar directivity pattern with milder decay at the extremes of the dipolar pattern. In addition, the $S = 0.2R$ case radiates higher noise compared to other tandem cases, whereas the $S = 0.6R$ case radiates less. Although not shown here for brevity, at $\mu = 0.3$, the $S = 0.6R$ case radiates as low as the single rotor case. A similar behaviour is evident for the results obtained on the side plane, Fig. 5, with two significant differences to be underlined. First, at static condition, $\mu = 0$ (Fig. 5(a)), unlike other cases, the directivity pattern displays a dipolar pattern. Secondly, the reduced far-field noise level for the $S = 0.6R$ case on the polar array at $\mu = 0.3$ takes a different form, where a reduced level of far-field noise $120^\circ < \phi < 180^\circ$ is accompanied by a significant increase at $180^\circ < \phi < 240^\circ$. Moreover, at this advance ratio, the $S = 0.2R$ case also radiates less noise for high ϕ angles than the single rotor case.

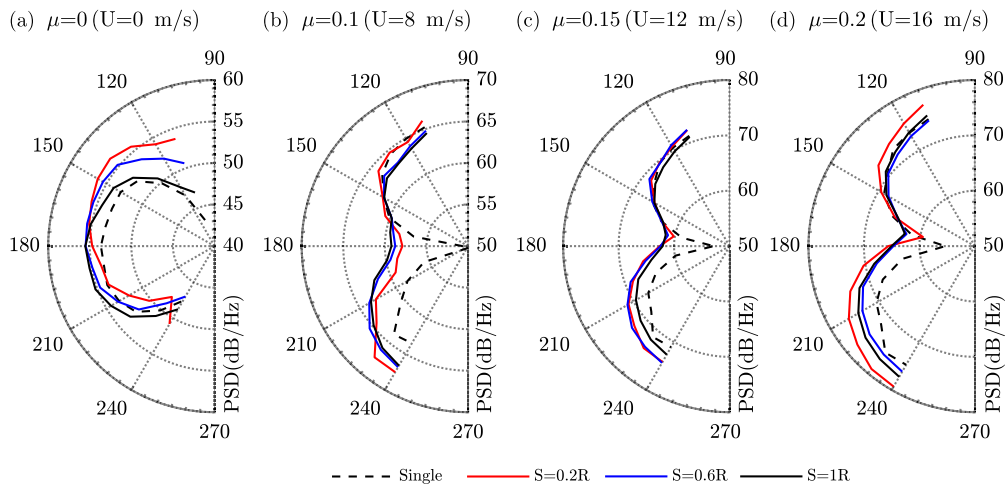


Fig. 9. 1stBPF directivity on the side array for separation distances of $S = 0.2R, 0.6R$ and $1R$ in comparison to single rotor results at advance ratios of (a) $\mu = 0$ (0 m/s), (b) $\mu = 0.1$ (8 m/s), (c) $\mu = 0.15$ (12 m/s) and (d) $\mu = 0.2$ (16 m/s).

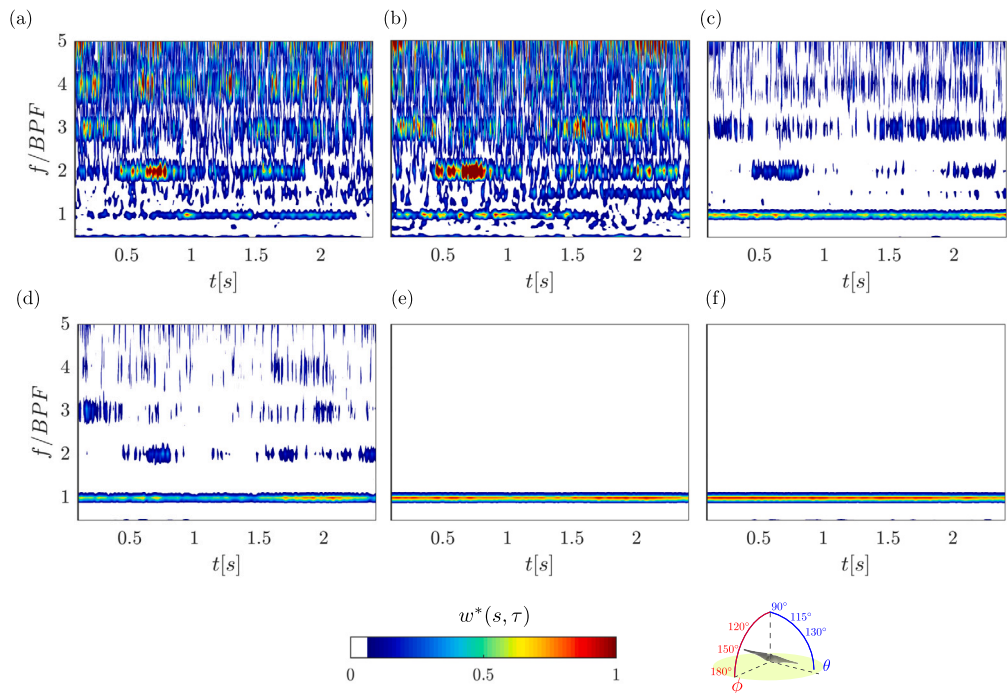


Fig. 10. Normalized wavelet scalograms for the single rotor case calculated for far-field noise measured on the polar array at (a) $\theta = 90^\circ$, (b) $\theta = 115^\circ$, and (c) $\theta = 130^\circ$, and obtained on the side-array at (d) $\phi = 120^\circ$, (e) $\phi = 150^\circ$, and (f) $\phi = 180^\circ$ at an advance ratio of $\mu = 0$ ($U = 0$ m/s).

3.3. Time-frequency analysis

Until this point, the effect of separation distance on the directivity, noise spectra and broadband noise of a tandem rotor configuration is analysed and discussed by relying on methods based on the Fourier Transform, i.e., power spectral density. The time-frequency analysis of the noise allows us to investigate the time-dependent nature of the radiated frequencies, providing a more detailed understanding of the noise characteristics. The time-dependent analysis may help to reveal both the intermittent nature and amplitude modulations of the noise. Although some contradictory results are presented in the literature [61,62], it is shown to influence annoyance perception of the noise. This study doesn't aim to address annoyance directly; however, the data herein may help for further studies in annoyance modelling. This section will address the temporal behaviour of the radiated noise by applying wavelet analysis following the methodology explained in Sec. 2.

Fig. 10 displays the normalized wavelet scalogram at $\mu = 0$ for the data obtained at three microphone locations for both the polar and side array. The wavelet analysis is presented for $\theta = 90^\circ, 115^\circ$ and 130° on the polar array (Fig. 10a, b and c) and for $\phi = 120^\circ, 150^\circ$ and 180° on the side array (Fig. 10d, e and f). The frequency axis is normalized with blade passage frequency to ease the interpretation of the data. Before delving into discussions, it is essential to note that periodic signals result in continuous lines in the scalograms [63]. The results from the wavelet analysis demonstrate a few important points to underline. Considering the results for the polar array, the scalogram results show that the noise radiated towards $\theta = 90^\circ$, Fig. 10a, at the 1st BPF is slightly intermittent with amplitude modulation. However, as the observation angle moves downstream, the noise radiation becomes continuous, Figs. 10b and c. Furthermore, an intermittent and high amplitude 2nd BPF is evident towards $\theta = 90^\circ$ and 115° , which weakens at $\theta = 130^\circ$. On the side array, the wavelet results show a significantly dominant continuous 1st

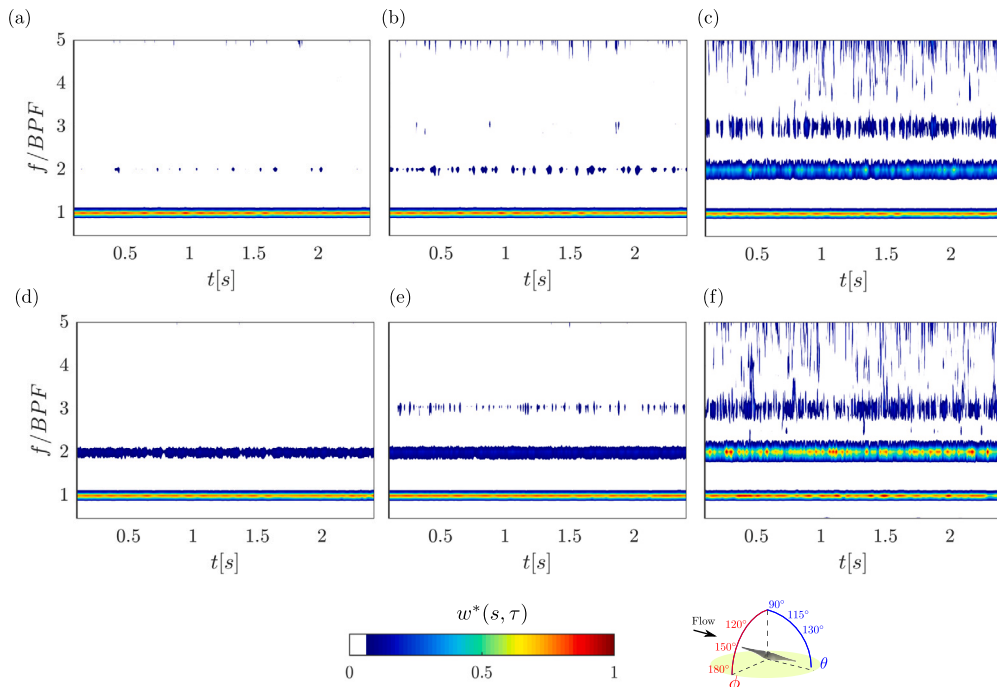


Fig. 11. Normalized wavelet scalograms for the single rotor case calculated for far-field noise measured on the polar array at (a) $\theta = 90^\circ$, (b) $\theta = 115^\circ$, and (c) $\theta = 130^\circ$, and measured on the side-array at (d) $\phi = 120^\circ$, (e) $\phi = 150^\circ$, and (f) $\phi = 180^\circ$ at an advance ratio of $\mu = 0.15$ ($U = 12$ m/s).

BPF towards the plane of rotation, $\phi = 180^\circ$ (Fig. 10f). It is also worth noting that the scalogram results show less dependency on the radiation angle on the side array. The presence of inflow has notable effects on the wavelet results, as evident in Fig. 11. The intermittent noise radiation at 1st BPF towards the top array in hover, Fig. 10 completely evolves into a periodic dominant radiation. This periodic behaviour is also observed in the side array results across all angles. Furthermore, the results suggest strong periodic radiation at the 2nd BPF, which might be due to the increased steady loading on the blades, considering that the 1st BPF and 2nd BPF emerges mostly due to steady loading [64,65]. It is crucial to underline that directivity patterns or spectral plots obtained employing Fourier Series analysis in Figs. 8 and 9 were not able to display the intermittent nature of the emitted noise, which is a significant factor of annoyance [66].

Following the discussions on the time-frequency analysis for a single rotor, the results regarding tandem configurations are now presented in Figs. 12 and 13. Fig. 12 displays normalized wavelet scalogram results for separation distances of $S = 0.2R$, $0.6R$ and $S = 1R$ for the polar array microphones at $\theta = 90^\circ$ [Fig. 12(a-c)] and $\theta = 130^\circ$ [Fig. 12(d-f)] at hovering conditions, $\mu = 0$. The results obtained from the microphone at $\theta = 90^\circ$ provide valuable insights into the effect of separation distance on the noise characteristics in tandem configurations compared to the single rotor case. For the $S=0.2R$ case, the normalized wavelet scalogram results suggest nearly-periodic noise radiation at the 1st BPF with amplitude modulation. Additionally, intermittent radiations with strong amplitude modulation at the BPF harmonics are evident. This pattern is similar to the results observed for the $S=1R$ case. However, for the $S=0.6R$ case, the scalogram suggests strongly intermittent 1st BPF noise radiation, as indicated by the separated islands of intermittent regions. Furthermore, the contribution from higher BPF harmonics is weaker compared to the results of the other cases. The intermittent nature of the noise becomes more widespread at higher frequencies, as evidenced by the presence of discontinuous patches of increased energy spots for all cases.

Further downstream on the polar array, i.e., $\theta = 130^\circ$, a different picture can be observed, which reinforces the fact that interpretation of the directivity and spectra plots are not sufficient to explain the nature

of the radiated noise shows temporal variations as well as a spatial dependency (directivity). When the rotors are at a minimum distance, $S = 0.2R$, the noise radiation at the 1st BPF is slightly intermittent with significant amplitude modulation. Although the intermittency pattern is similar to $\theta = 90^\circ$ for the noise radiated at the 2nd BPF and 3rd BPF, the contribution from 3rd BPF significantly increases at $\theta = 130^\circ$, as indicated by the presence of high-intensity energy spots in the scalogram. As discussed for the results at $\theta = 90^\circ$, the results of the $S=1R$ case show similarity with the $S=0.2$ case, with notably lower amplitudes. Furthermore, for the $S=0.6$ case, the intermittent nature at the 1st BPF becomes clearer. With the presence of an incoming flow as displayed in Fig. 13, at $\mu = 0.15$, the scattered low energy intermittent events at higher frequencies diminish. The increase of the blade loading increases the contribution of the 1st and 2nd BPF. At both $\phi = 90^\circ$ and $\phi = 130^\circ$, relatively long duration strong intermittent events emerge at $S=0.2R$ at the 1st BPF, with weak intermittent contributions from 2nd BPF. At $S=0.6R$, the long-duration intermittent events evolve into short-duration events, as indicated by multiple energy islands in the scalogram. Further increase in the separation distance to $S=1R$ recovers the time-dependent energy distribution similar to that of the $S=0.2R$ case with a periodic 1st BPF. The changes observed in the steady loading behaviour may be related to complex wake interactions between two rotors. For brevity, the time-frequency analysis of the side array is provided in the supplementary document in Figs. S3 and S4 for $\mu = 0$ and $\mu = 0.15$, respectively. The results show that the amplitude modulation and intermittency characteristics presented resemble those of the polar array results.

4. Conclusion

This study presents an experimental investigation of the noise radiation characteristics of two rotors in a tandem configuration under both hover and edge-wise flight conditions, with a focus on the effect of the influence of separation distance. The far-field noise measurement was conducted on two arrays for both tandem and single-rotor cases with a fixed rotational speed. The far-field noise results were comprehensively analysed and presented in terms of OASPL directivity, frequency-dependent energy spectra and temporal characteristics.

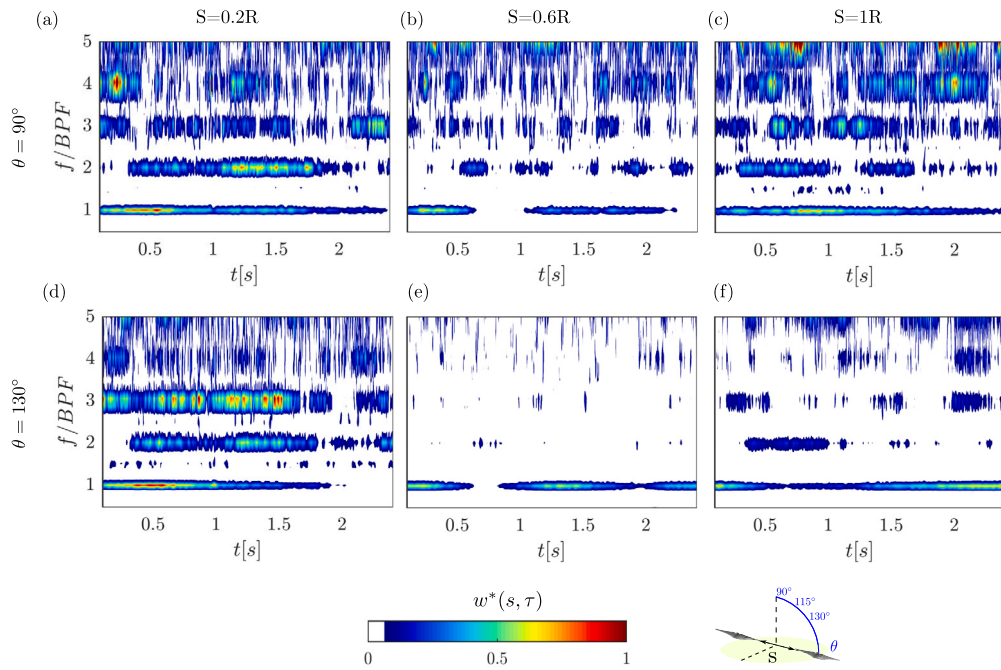


Fig. 12. Normalized wavelet scalograms for tandem configurations calculated for far-field noise measured on the polar array at $\theta = 90^\circ$ (top-row) and $\theta = 130^\circ$ (bottom-row). The results are presented for separation distances of (a,d) $S = 0.2R$, (b,e) $S = 0.6R$, and (c,f) $S = 1R$ at $\mu = 0$ ($U = 0$ m/s).

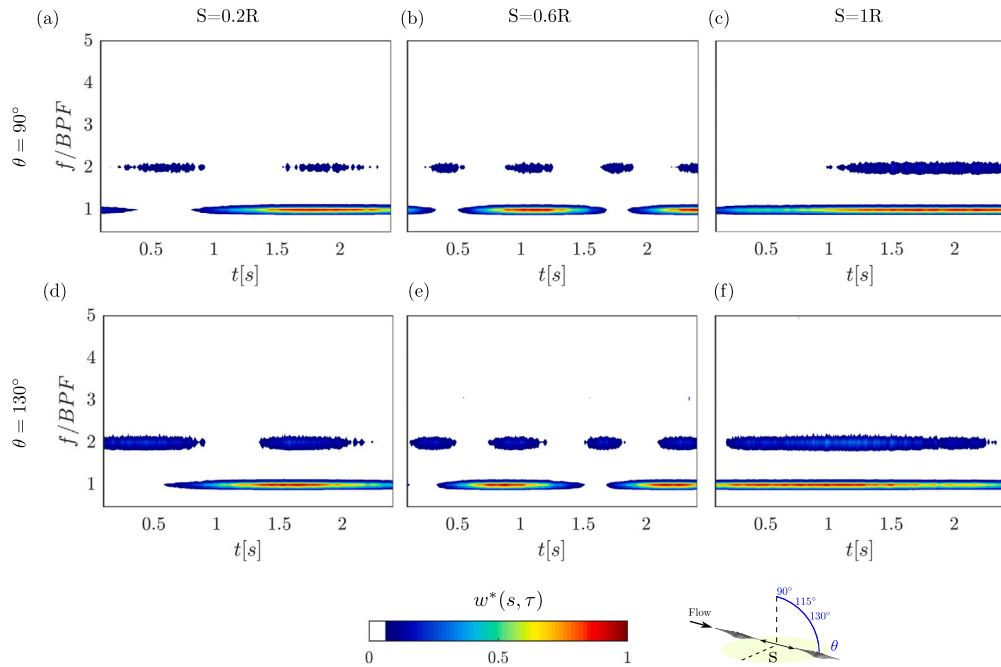


Fig. 13. Normalized wavelet scalograms for tandem configurations calculated for far-field noise measured on the polar array at $\theta = 90^\circ$ (top-row) and $\theta = 130^\circ$ (bottom-row). The results are presented for separation distances of (a,d) $S = 0.2R$, (b,e) $S = 0.6R$, and (c,f) $S = 1R$ at $\mu = 0.15$ ($U = 12$ m/s).

The OASPL results revealed similar directivity patterns for all cases, but the tandem configurations exhibited significantly higher noise levels compared to the single case. Among the cases with different separation distances, $S=0.2R$ radiated the highest noise, and $S=0.6R$ case radiated the lowest noise on both measurement arrays. The narrowband behaviour showed significantly increased PSD levels at the 1st BPF for the shortest separation distance, corroborating with the 1st BPF directivity results. The increased level of broadband noise at both high and low frequencies indicates the increased level of interaction of rotors. The results show that as the advance ratio increases, the tandem configurations radiate higher noise at lower frequencies on a broader bandwidth

than the single rotor. The low-frequency energy content increase can be attributed to contributions from the wake and complex wake interactions, which is consistent with the findings of Mankbadi et al. [45]. Furthermore, an increase in the low-to-mid frequency broadband noise may also emanate from an increase in blade self-noise, i.e., trailing edge noise and turbulent boundary layer noise, due to an increased advance ratio [25]. Further studies in the flow field are required to fully explore the underpinning mechanism, which is beyond the scope of this manuscript. The findings show an envelope of parameters that can minimize the radiated broadband noise. Finally, the time-frequency analysis revealed the intermittent nature and the amplitude modulation of the

radiated noise at the 1st and 2nd BPF. The wavelet results show that 1st BPF becomes strongly intermittent at $S=0.6R$ case, generating the lowest OASPL. Although the current study shows the complex nature of the noise radiation for a simple two-rotor tandem configuration, there exists a vast design space for future UAM layouts. To better understand the underlying physics of the observed behaviours, further work on detailed flow field analysis is recommended as a follow-up study, which can provide a deeper understanding of the noise generation mechanism and aid in designing and optimizing the urban air mobility systems.

CRedit authorship contribution statement

Alper Celik: Conceptualization, Data curation, Formal analysis, Investigation, Methodology, Project administration, Software, Visualization, Writing – original draft, Writing – review & editing. **Nur Syafiqah Jamaluddin:** Conceptualization, Data curation, Formal analysis, Investigation, Methodology, Software. **Kabilan Baskaran:** Data curation, Formal analysis, Investigation, Methodology. **Stefano Meloni:** Formal analysis, Writing – review & editing. **Djamel Rezgui:** Conceptualization, Funding acquisition, Methodology, Supervision, Writing – review & editing. **Mahdi Azarpeyvand:** Conceptualization, Funding acquisition, Methodology, Supervision, Writing – review & editing.

Declaration of competing interest

The authors declare that they have no known competing financial interests or personal relationships that could have appeared to influence the work reported in this paper.

Data availability

Data will be made available on request.

Acknowledgement

The first author would like to acknowledge the EPSRC (Engineering and Physical Sciences Research Council) for post-doctoral sponsorship at the University of Bristol from June 2020 to December 2021 (Grant No. EP/S013024/1). The second author would like to acknowledge the financial support of Majlis Amanah Rakyat Malaysia. All authors would like to acknowledge Horizon 2020 research and innovation programme under grant agreement number 882842 (SilentProp project).

Appendix A. Supplementary material

Supplementary material related to this article can be found online at <https://doi.org/10.1016/j.apacoust.2024.110053>.

References

- [1] EASA. Study on the societal acceptance of urban air mobility in Europe. Tech. rep. European Union Aviation Safety Agency (EASA); 2021.
- [2] Rizzi SA, Huff DL, Boyd DD, Bent P, Henderson BS, Pascioni KA, et al. Urban air mobility noise: current practice, gaps, and recommendations. Tech. rep., NASA/TP-20205007433. NASA; 2020.
- [3] Yunus F, Casalino D, Avallone F, Ragni D. Efficient prediction of urban air mobility noise in a vertiport environment. *Aerosp Sci Technol* 2023;139:108410. <https://doi.org/10.1016/j.ast.2023.108410>.
- [4] Hanson L, Jawahar HK, Vemuri SS, Azarpeyvand M. Experimental investigation of propeller noise in ground effect. *J Sound Vib* 2023;559:117751. <https://doi.org/10.1016/j.jsv.2023.117751>.
- [5] Smith MJT. *Aircraft noise*. Cambridge aerospace series. Cambridge University Press; 1989.
- [6] Filippone A. Aircraft noise prediction. *Prog Aerosp Sci* 2014;68:27–63. <https://doi.org/10.1016/j.paerosci.2014.02.001>.
- [7] George AR. Helicopter noise: state-of-the-art. *J Aircr* 1978;15(11):707–15. <https://doi.org/10.2514/3.58436>.
- [8] Brentner K, Farassat F. Helicopter noise prediction: the current status and future direction. *J Sound Vib* 1994;170(1):79–96. <https://doi.org/10.1006/jsvi.1994.1047>.
- [9] Bohorquez F, Samuel P, Sirohi J, Pines D, Rudd L, Perel R. Design, analysis and hover performance of a rotary wing micro air vehicle. *J Am Helicopter Soc* 2003;48(2):80–90. <https://doi.org/10.4050/JAHS.48.80>.
- [10] Hein BR, Chopra I. Hover performance of a micro air vehicle: rotors at low Reynolds number. *J Am Helicopter Soc* 2007;52(3):254–62. <https://doi.org/10.4050/JAHS.52.254>.
- [11] Grande E, Ragni D, Avallone F, Casalino D. Laminar separation bubble noise on a propeller operating at low Reynolds numbers. *AIAA J* 2022;60(9):5324–35. <https://doi.org/10.2514/1.J061691>.
- [12] Romani G, Grande E, Avallone F, Ragni D, Casalino D. Performance and noise prediction of low-Reynolds number propellers using the lattice-Boltzmann method. *Aerosp Sci Technol* 2022;125:107086. <https://doi.org/10.1016/j.ast.2021.107086>. sI: DICUAM 2021.
- [13] Candeloro P, Ragni D, Pagliaroli T. Small-scale rotor aeroacoustics for drone propulsion: a review of noise sources and control strategies. *Fluids* 2022;7(8). <https://doi.org/10.3390/fluids7080279>.
- [14] Leslie A, Wong KC, Auld D. Broadband noise reduction on a mini-uav propeller. in: 14th AIAA/CEAS Aeroacoustics Conference (29th AIAA Aeroacoustics Conference). Vancouver, British Columbia, Canada. AIAA 2008-3069. <https://arc.aiaa.org/doi/abs/10.2514/6.2008-3069>.
- [15] Deters RW, Krishnan GKA, Selig MS. Reynolds number effects on the performance of small-scale propellers. in: 32nd AIAA Applied Aerodynamics Conference. Atlanta, GA. AIAA 2014-2151. <https://arc.aiaa.org/doi/abs/10.2514/6.2014-2151>.
- [16] Deters RW, Ananda GK, Selig MS. Slipstream measurements of small-scale propellers at low Reynolds numbers. in: 33rd AIAA Applied Aerodynamics Conference. Dallas, TX. AIAA 2015-2265. <https://arc.aiaa.org/doi/abs/10.2514/6.2015-2265>.
- [17] Brandt J, Selig M. Propeller performance data at low Reynolds numbers. in: 49th AIAA Aerospace Sciences Meeting including the New Horizons Forum and Aerospace Exposition. Orlando, FL. AIAA 2011-1255. <https://arc.aiaa.org/doi/abs/10.2514/6.2011-1255>.
- [18] Go Y-J, Bae J-H, Ryi J, Choi J-S, Lee C-R. A study on the scale effect according to the Reynolds number in propeller flow analysis and a model experiment. *Aerospac* 2022;9(10). <https://doi.org/10.3390/aerospac9100559>.
- [19] Morfey C. Rotating blades and aerodynamic sound. *J Sound Vib* 1973;28(3):587–617. [https://doi.org/10.1016/S0022-460X\(73\)80041-0](https://doi.org/10.1016/S0022-460X(73)80041-0).
- [20] Brentner KS, Farassat F. Modeling aerodynamically generated sound of helicopter rotors. *Prog Aerosp Sci* 2003;39(2):83–120. [https://doi.org/10.1016/S0376-0421\(02\)00068-4](https://doi.org/10.1016/S0376-0421(02)00068-4).
- [21] Kim YN, George AR. Trailing-edge noise from hovering rotors. *AIAA J* 1982;20(9):1167–74. <https://doi.org/10.2514/3.51176>.
- [22] Chen H-N, Brentner KS, Lopes LV, Horn JF. An initial analysis of transient noise in rotorcraft maneuvering flight. *Int J Aeroacoust* 2006;5(2):109–38. <https://doi.org/10.1260/147547206777629853>.
- [23] Celik A, Jamaluddin NS, Baskaran K, Rezgui D, Azarpeyvand M. Aeroacoustic performance of rotors in tandem configuration. in: AIAA Aviation 2021 Forum, Virtual Event, AIAA 2021-2282. <https://arc.aiaa.org/doi/10.2514/6.2021-2282>.
- [24] Johnson W. *Noise*. Cambridge aerospace series. Cambridge University Press; 2013. p. 493–544.
- [25] Akiwate DC, Parry AB, Joseph P, Paruchuri CC. On the balance between the tonal and broadband noise of uninstalled propellers. in: AIAA Aviation 2021 Forum, VIRTUAL EVENT, AIAA 2021-2308. <https://doi.org/10.2514/6.2021-2308>.
- [26] Li SK, Lee S. Prediction of urban air mobility multirotor vtol broadband noise using ucd-quietfly. *J Am Helicopter Soc* 2021;66(3):1–13. <https://doi.org/10.4050/JAHS.66.032004>.
- [27] Goldschmidt J, Tingle H, Ifgu PG, Miller SA, Ukeiley LS, Goldman B, et al. Acoustics and forces from an isolated rotor system. <https://doi.org/10.2514/6.2022-2530>.
- [28] Pang E, Cambray A, Rezgui D, Azarpeyvand M, Ali SAS. Investigation towards a better understanding of noise generation from uav propellers. in: 2018 AIAA/CEAS Aeroacoustics Conference. Atlanta, GA. AIAA 2018-3450. <https://doi.org/10.2514/6.2018-3450>.
- [29] Moslem F, Masdari M, Fedir K, Moslem B. Experimental investigation into the aerodynamic and aeroacoustic performance of bioinspired small-scale propeller platforms. *Proc Inst Mech Eng, G J Aerosp Eng* 2023;237(1):75–90. <https://doi.org/10.1177/09544100221091322>.
- [30] Wang H, Zang B, Celik A, Rezgui D, Azarpeyvand M. An experimental investigation of propeller noise in forward flow. in: 25th AIAA/CEAS Aeroacoustics Conference. Delft, the Netherlands. AIAA 2019-2620. <https://doi.org/10.2514/6.2019-2620>.
- [31] Jamaluddin NS, Celik A, Baskaran K, Rezgui D, Azarpeyvand M. Aeroacoustic performance of propellers in turbulent flow. in: AIAA Aviation 2021 Forum, VIRTUAL EVENT, AIAA 2021-2188. <https://doi.org/10.2514/6.2021-2188>.
- [32] Jamaluddin NS, Celik A, Baskaran K, Rezgui D, Azarpeyvand M. Experimental analysis of a propeller noise in turbulent flow. *Phys Fluids* 2023;35(7):075106. <https://doi.org/10.1063/5.0153326>.
- [33] Zawodny NS, Boyd DDJ, Burley CL. Acoustic characterization and prediction of representative, small-scale rotary-wing unmanned aircraft system components. In: *American helicopter society (AHS) annual forum*; 2020.
- [34] NASA. Nasa urban air mobility (UAM) reference vehicles. <https://sacd.larc.nasa.gov/uam-refs/>, 2023.
- [35] Shukla D, Komerath N. Multirotor drone aerodynamic interaction investigation. *Drones* 2018;2(4). <https://doi.org/10.3390/drones2040043>.

- [36] Shukla D, Hiremath N, Komerath NM. Low Reynolds number aerodynamics study on coaxial and quad-rotor. in: 2018 Applied Aerodynamics Conference. Atlanta, GA. AIAA 2018-4118. <https://doi.org/10.2514/6.2018-4118>.
- [37] Zhou W, Ning Z, Li H, Hu H. An experimental investigation on rotor-to-rotor interactions of small uav propellers. in: 35th AIAA Applied Aerodynamics Conference. Denver, CO. AIAA-2017-3744. <https://doi.org/10.2514/6.2017-3744>.
- [38] Chae S, Lee S, Kim J. Effects of rotor-rotor interaction on the wake characteristics of twin rotors in axial descent. *J Fluid Mech* 2022;952:A31. <https://doi.org/10.1017/jfm.2022.913>.
- [39] Misiorowski M, Gandhi F, Oberai AA. Computational study on rotor interactional effects for a quadcopter in edgewise flight. *AIAA J* 2019;57(12):5309–19. <https://doi.org/10.2514/1.J058369>.
- [40] de Vries R, van Arnhem N, Sinnige T, Vos R, Veldhuis LL. Aerodynamic interaction between propellers of a distributed-propulsion system in forward flight. *Aerosp Sci Technol* 2021;118:107009. <https://doi.org/10.1016/j.ast.2021.107009>.
- [41] Tinney CE, Sirohi J. Multirotor drone noise at static thrust. *AIAA J* 2018;56(7):2816–26. <https://doi.org/10.2514/1.J056827>.
- [42] Poggi C, Bernardini G, Gennaretti M, Camussi R. Scalability of Mach number effects on noise emitted by side-by-side propellers. *Appl Sci* 2022;12(19). <https://doi.org/10.3390/app12199507>.
- [43] Bu H, Wu H, Bertin C, Fang Y, Zhong S. Aerodynamic and acoustic measurements of dual small-scale propellers. *J Sound Vib* 2021;511:116330. <https://doi.org/10.1016/j.jsv.2021.116330>.
- [44] Reed N, Cuppoletti DR. Implications of rotor-rotor interaction in noise generation of UAM vehicles with counter-rotating configurations. <https://doi.org/10.2514/6.2022-2168>.
- [45] Mankbadi RR, Afari SO, Golubev VV. High-fidelity simulations of noise generation in a propeller-driven unmanned aerial vehicle. *AIAA J* 2021;59(3):1020–39. <https://doi.org/10.2514/1.J059117>.
- [46] Mayer YD, Jawahar HK, Szöke M, Ali SAS, Azarpeyvand M. Design and performance of an aeroacoustic wind tunnel facility at the university of Bristol. *Appl Acoust* 2019;155:358–70. <https://doi.org/10.1016/j.apacoust.2019.06.005>.
- [47] Welch P. The use of fast Fourier transform for the estimation of power spectra: a method based on time averaging over short, modified periodograms. *IEEE Trans Audio Electroacoust* 1967;15(2):70–3.
- [48] Camussi R, Meloni S. On the application of wavelet transform in jet aeroacoustics. *Fluids*, vol. 6. 2021.
- [49] Micci GL, Camussi R, Meloni S, Bogey C. Intermittency and stochastic modeling of low- and high-Reynolds-number compressible jets. *AIAA J* 2022;60(3):1983–90. <https://doi.org/10.2514/1.J061128>.
- [50] Sorensen PN, Cuppoletti DR. Source noise mechanisms of co-rotating and counter rotating rotors in hover for air mobility applications. <https://doi.org/10.2514/6.2022-2879>.
- [51] Landström U, Åkerlund E, Kjellberg A, Tesarz M. Exposure levels, tonal components, and noise annoyance in working environments. *Environ Int* 1995;21(3):265–75. [https://doi.org/10.1016/0160-4120\(95\)00017-F](https://doi.org/10.1016/0160-4120(95)00017-F).
- [52] Gourdain N, Jardin T, Serre R, Prothin S, Moschetta J-M. Application of a lattice Boltzmann method to some challenges related to micro-air vehicles. *Int J Micro Air Veh* 2018;10(3):285–99. <https://doi.org/10.1177/1756829318794174>.
- [53] Lee A, Aravamudan K, Bauer P, Harris W. An experimental investigation of helicopter rotor high frequency broadband noise. in: 4th Aeroacoustics Conference. Atlanta, GA. AIAA 1977-1339. <https://doi.org/10.2514/6.1977-1339>.
- [54] Humbad N, Harris W. Model rotor low frequency broadband noise at moderate tip speeds. in: 6th Aeroacoustics Conference, Hartford, CT, AIAA 1980-1013. <https://doi.org/10.2514/6.1980-1013>.
- [55] Humbad N, Harris W. Tip geometry effects on the model helicopter rotor low frequency broadband noise. in: 7th Aeroacoustics Conference, Palo Alto, CA, AIAA 1981-2003. <https://doi.org/10.2514/6.1981-2003>.
- [56] Kingan M, Blandeau V, Tester B, Joseph P, Parry A. Relative importance of open rotor tone and broadband noise sources. In: 17th AIAA/CEAS aeroacoustics conference (32nd AIAA aeroacoustics conference), Portland, OR, AIAA 2011-2763; 2011.
- [57] Kingan M, Ekoule C, Parry AB, Britchford K. Analysis of advanced open rotor noise measurements. In: 20th AIAA/CEAS aeroacoustics conference, Atlanta, GA, AIAA 2014-2745; 2014. <https://doi.org/10.2514/6.2014-2745>.
- [58] Stephens DB, Vold H. Order tracking signal processing for open rotor acoustics. *J Sound Vib* 2014;333(16):3818–30.
- [59] McKay RS, Kingan MJ, Go ST, Jung R. Experimental and analytical investigation of contra-rotating multi-rotor uav propeller noise. *Appl Acoust* 2021;177:107850.
- [60] Moreau S, Roger M. Effect of angle of attack and airfoil shape on turbulence-interaction noise. in: 11th AIAA/CEAS Aeroacoustics Conference. Monterey, California, AIAA 2005-2973. <https://doi.org/10.2514/6.2005-2973>.
- [61] Dornic S, Laaksonen T. Continuous noise, intermittent noise, and annoyance. *Percept Mot Skills* 1989;68(1):2928031. <https://doi.org/10.2466/pms.1989.68.1.11>.
- [62] Murphy E, King EA. Chapter 3 - environmental noise and health. In: Murphy E, King EA, editors. *Environmental noise pollution*. Boston: Elsevier; 2014. p. 51–80.
- [63] Meloni S, de Paola E, Grande E, Ragni D, Stoica LG, Marco AD, et al. A wavelet-based separation method for tonal and broadband components of low Reynolds-number propeller noise. *Meas Sci Technol* 2023;34(4):044007. <https://doi.org/10.1088/1361-6501/acb071>.
- [64] Grande E, Romani G, Ragni D, Avallone F, Casalino D. Aeroacoustic investigation of a propeller operating at low Reynolds numbers. *AIAA J* 2022;60(2):860–71. <https://doi.org/10.2514/1.J060611>.
- [65] Kim DH, Moon YJ. Aerodynamic analyses on the steady and unsteady loading-noise sources of drone propellers. *Int J Aeronaut Space Sci* 2019;20(3):611–9. <https://doi.org/10.1007/s42405-019-00176-3>.
- [66] Gwak DY, Han D, Lee S. Sound quality factors influencing annoyance from hovering uav. *J Sound Vib* 2020;489:115651. <https://doi.org/10.1016/j.jsv.2020.115651>.